Temporal-Spatial-Resolved Lasing Dynamics in Customized Solution Grown Perovskite Single-Crystal Microcavities

Peipei Ma, Lihe Yan,* Jinhai Si, Tianyu Huo, Zhenqiang Huang, Wenjiang Tan, Jin Xu, and Xun Hou

Single-crystal halide perovskites are among the most promising semiconductor candidates for highly efficient optoelectronic devices due to their higher stability against moisture and light radiation and lower trap density than their polycrystalline counterparts. In this work, single-crystal MAPbBr$_3$ microcavities with controllable geometries and sizes are fabricated using a template-limited method combined with an anti-solvent diffusion growth method. The single-crystal microcavities emit lasers around 550 nm under femtosecond laser excitation, with a lasing threshold of ≈35 μJ cm^{-2} and a quality factor of 1135, as well as excellent long-term operation stability. The temporal-spatial evolution of the lasing process in an individual microcavity is achieved by the microscopic optical Kerr-gating technique. The temporal behaviors including pulse duration and build-up time, emission spectra shift, and lasing mode evolution as a function of pump fluence are unveiled, and the complex relationship between the light-induced carrier dynamics and lasing properties is clarified. Spatial heterogeneous lasing dynamics are also observed in an individual microdisk, which is attributed to the non-uniform optical losses and carrier densities driven by structural imperfections. This study can provide a fabrication strategy for perovskite on-chip optoelectronic devices, as well as a deeper understanding of the carrier-density-driven lasing dynamics in microcavities.

1. Introduction

Micro/nanolasers are important on-chip nanophotonic devices providing coherent light sources for the demands of higher integration, faster computing, and broader communication bandwidth.[1–6] Although kinds of materials have been explored

P. Ma, L. Yan, J. Si, T. Huo, Z. Huang, W. Tan, J. Xu, X. Hou
Key Laboratory for Physical Electronics and Devices of the Ministry of Education & Shaanxi Key Lab of Photonic Technique for Information,
School of Electronics Science & Engineering, Faculty of Electronic and Information Engineering
Xi'an Jiaotong University
Xi'an 710049, China
E-mail: liheyan@mail.xjtu.edu.cn
J. Xu
School of Electronics Engineering and Computer Science
Peking University
Beijing 100871, China

for the fabrication of on-chip coherent light sources,[7–11] achieving micro/nanoscale lasers with narrow linewidth, wide tunable wavelength range, and high stability remains a challenge. Recently, metal halide perovskites have emerged as competitive candidates for optoelectronic devices due to their facile solution-processable synthesis and unique photoelectric properties, including tunable emission across the visible spectrum, high fluorescence yield, long carrier diffusion length, and so on.[12] Due to these advantages, various perovskite micro/nanostructures, such as micro/nanocrystals and patterned polycrystalline films, have been proposed as effective resonator cavities for micro/nanolasers.[13]

Until now, the lasing properties of various perovskite micro/nanocrystals including nanoplates, microcubes, and microspheres have been studied, in which the self-organized intrinsic crystal interfaces functioned as natural reflectors of the resonators.[14–16] Benefitting from their superior stability against moisture, oxygen, light, and heat due to lower trap densities, single-crystal perovskites show better application potential than polycrystalline films in micro/nanolasers. However, the practical applications of single-crystal perovskites in devices have not progressed as expected. On one hand, the morphology of solution-synthesized micro/nanocrystals is highly determined by its intrinsic crystal structure, and the overall size differs significantly, which is adverse to the precise control of the lasing property. For this reason, some top-down fabrication technologies, such as electron beam lithography and focused ion beam etching, have been exploited for the precision machining of perovskite micro/nano lasers,[17,18] but the high cost has prevented their applications for mass production. Besides, the femtosecond laser fabrication technique has also been used for the processing of laser microcavities on perovskites, while the inevitable accompanied surface damage and amorphization could deteriorate the optical properties and stabilities of the devices.[19,20] Therefore, exploiting effective one-step customized synthesis of single-crystal perovskite microcavities without post-processing is necessary.

Besides the morphology and structure of the microcavities, the lasing properties are closely related to the light-induced carrier

density and dynamics, including recombination processes, hot-carrier relaxation processes, etc. Time-resolved emission spectroscopy can help to detect the lasing dynamics of the cavities and reveal the relation between the lasing and carrier properties. Some studies have made in-depth analyses of the lasing properties of perovskite microcavity in the spectrum and time domain. Andrew and co-workers regarded the blue-shifting of gain profile on the tens of picoseconds time scale as a signature for plasmon-coupled lasing from a non-degenerate electron-hole plasma, which figure out the lasing mechanism in individual $CsPbBr_3$ nanowire.[21] Wang and co-workers investigated the red-shifting in individual microplate at high excitation intensity and successfully suppressed this mode shifting using distributed Bragg reflectors to optimize the mode quality of microlasers.[22,23] At the same time, it is well recognized that local heterogenous photoresponse or electroresponse of perovskite grains would affect the performance of solar cell or LED devices, while these studies are lacking in micro/nanolasers. Therefore, it is necessary to investigate and understand the spatial characteristics of microcavity lasing.

In this paper, customized $MAPbBr_3$ microcavities are fabricated using a template-limited growth method. To control the grain size and the surface roughness of the cavities, a modified anti-solvent diffusion process is utilized. By reducing the reaction rate, nucleation sites at the interface between templates and solution are restrained, and clean and sharp borders of microcavities with steerable geometries and sizes are obtained. The single-crystal microcavities emit laser with a wavelength of ≈ 550 nm under 400 nm femtosecond laser excitation. The micro-lasers show a lasing threshold of ≈ 35 μJ cm^{-2}, and a quality factor (Q-factor) of 1135, as well as excellent long-term operation stability. Microscopic optical Kerr-gating measurement is used to study the emission dynamics of an individual microdisk. The emission dynamics, including temporal behaviors (pulse duration and build-up time), emission spectra shift, and lasing mode evolution as a function of pump fluence are observed. Moreover, we utilize the microscopic optical Kerr-gating image technique to bond the spatial morphology features and temporal lasing behaviors in an individual perovskite microdisk laser. The spatial heterogeneous lasing dynamics in an individual microdisk are observed, which are attributed to the non-uniform optical losses and photoexcited carrier densities driven by the structural imperfections of cavity sidewalls. This work probes and maps the spatial lasing dynamics in individual microdisks and provided ideas for the control of lasing behaviors in an ultrafast time scale in perovskite micro-lasers.

2. Results and Discussion

The schematic diagram of the single-crystal $MAPbBr_3$ microcavities fabrication process by template-limited and anti-solvent diffusion growth method is described in **Figure 1a** (for more details see Experimental Section). The spatially template-limited growth aims to customize the geometry of microcavities by restricting lateral crystallization forcefully. As shown in Figure 1b, $MAPbBr_3$ microcavities with diverse geometries and sizes are achieved. Flexible geometries can both support the Fabry–Pérot and whispering-gallery-mode resonators, and various sizes are

crucial to the management of free spectrum range (FSR). However, the interface between templates and solution usually acts as nucleation sites during the growth, which would introduce undesirable polycrystalline films, as has been reported previously and in our experiment result shown in Figure S1 (Supporting Information).[20,24,25] Anti-solvent diffusion growth is an effective solution for polycrystalline films.[26] Compared with removing the good solvent for $MAPbBr_3$ by annealing, the diffusion rate of the anti-solvent at room temperature is much slower, resulting in the reduction of nucleation density and deceleration of crystal growth rate. Sparse nucleation sites grow at a slow rate to eventually obtain single-crystal rather than polycrystalline films. Moreover, the slow growth rate makes the thickness of single-crystal microcavities more controllable by regulating the growth time. According to the statistical data (Figure S2a, Supporting Information), the thickness of microcavities ranges from 102 to 226 nm, corresponding to the different colors of microcavities under the optical microscope (Figure 1b).

Details of single-crystal microdisks are measured by tilted scanning electron microscope (SEM) and atomic force microscopy (AFM). The SEM images in Figure 1c show that the pristine top surface of the microdisk is smooth and clean, and the related calculated root-mean-square surface roughness is about 5 nm in a scan area of 100 μm^2, as shown in Figure S2b (Supporting Information). This is due to the slow and balanced growth rate of each location on the surface supported by the anti-solvent diffusion growth method. A smooth and clean surface would restrain light scattering and enhance the light confinement ability of resonators. Besides, hinging on the accurate photolithographic templates, the sidewalls of single-crystal microdisk showed sharp profiles as shown in the enlarged SEM image (Figure 1c). Sharp and vertical sidewalls are beneficial to reduce the number of competing modes of laser.

To characterize the single-crystal nature and crystal structure of the $MAPbBr_3$ microcavities, X-ray diffraction (XRD) pattern is given in Figure 1d. The sharp diffraction peaks at $15.02°$, $30.20°$, $45.96°$, and $62.70°$ are assigned to (001), (002), (003), and (004) planes of $MAPbBr_3$ cubic structure.[27,28] The full width at half maximum (FWHM) of (001) peak is calculated as $0.062°$ in Figure S3 (Supporting Information), also indicating good crystalline quality.

To investigate the optical properties including photoluminescence and lasing features of individual $MAPbBr_3$ single-crystal microcavity, a home-built micro-PL set-up (Figure S4, Supporting Information) is equipped with a femtosecond laser source (central wavelength: 800 nm, pulse width: 50 fs, and repetition rates: 1 kHz). With the frequency-doubling 400 nm pulse laser as the excitation light, bright yellow-green emission centered at 537 nm with a Gaussian distribution and FWHM of 28 nm is achieved as given in Figure 1e. The absorbance of $MAPbBr_3$ single-crystals with thicknesses >10 μm displays a sharp band-edge cutoff at 534 nm, suggesting fewer defect states in the material.[29] The slight red-shift of the absorption band edge compared with films is attributed to the below-bandgap absorption.[30] Furthermore, the carrier recombination process in $MAPbBr_3$ single-crystal is revealed through time-resolution photoluminescence (TRPL) with an excitation wavelength of 375 nm. As shown in Figure 2f, the decay process of the PL can be well fitted using a tri-exponential function with a fast lifetime of 3.47 ns,

ADVANCED
SCIENCE NEWS

www.advancedsciencenews.com
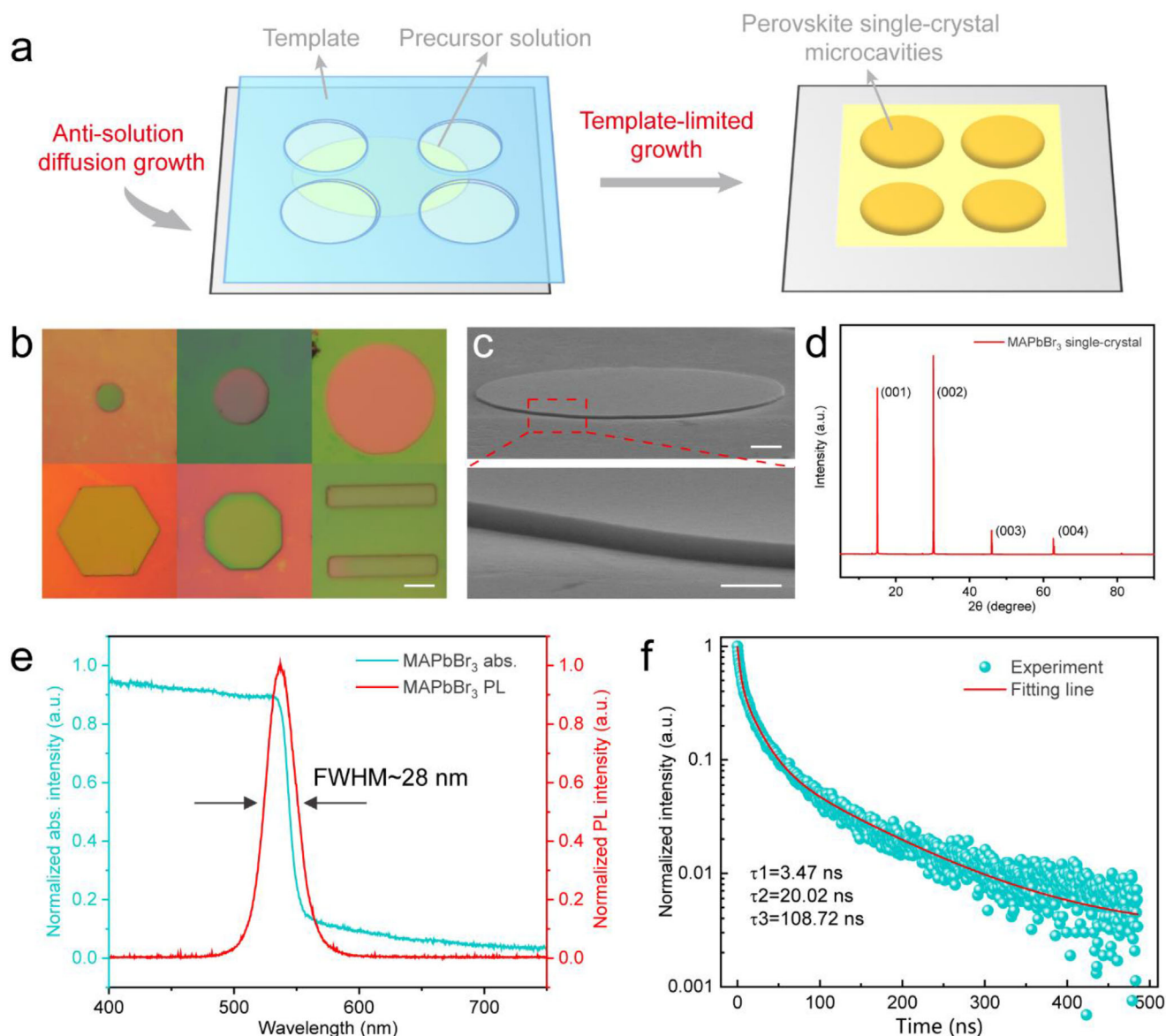
LASER
& PHOTONICS
REVIEWS

www.lpr-journal.org

Figure 1. a) Schematic illustration of single-crystal perovskite microcavities fabrication processes. b) Optical microscope images of the fabricated single-crystal perovskite microcavities. Scale bar, 5 µm. c) SEM images of single-crystal perovskite microdisk. Scale bar, 2 µm and 500 nm. d) XRD pattern of single-crystal MAPbBr$_3$. e) Absorbance and photoluminescence spectra of single-crystal MAPbBr$_3$. f) TRPL data and fitting curve of single-crystal MAPbBr$_3$.

as well as two slow lifetimes of 20.02 and 108.72 ns, respectively. The results are in accordance with those reported in previous works,[31,32] while these three decay processes can be attributed to band edge recombination, bulky recombination, and surface recombination, respectively.

To measure the lasing features of the microdisk, the laser beam size is optimized to ensure a uniform excitation on the microdisk by adjusting the distance between the sample and the microscope objective. Representative emission spectra of individual MAPbBr$_3$ single-crystal microdisk with 20 µm diameter as a function of pump fluence (φ, pulse energy per unit area) at room temperature are shown in **Figure 2**a. At low pump fluence below the lasing threshold, a broad spontaneous emission

peaked at 536.4 nm with an FWHM of 24.5 nm is observed. As the pump fluence increases, new sharp stimulated emission peaks appear and rise dramatically at the lower-energy band-tail of the spontaneous emission. The intensity is orders of magnitude higher than the spontaneous emission, indicating multimode lasing generated in the microdisk. The dependence of output intensity and FWHM on pump fluence are given in Figure 2b (see Figure S5, Supporting Information, for initial emission spectra). It can be seen that a superlinear increase of output intensity and linewidth narrowing occur simultaneously, giving a lasing threshold (P_{th}) of ≈35 µJ cm^{-2}. For the linewidth above the threshold, the Q-factors could get a maximum of 1135. The fluorescence image of the microdisk with pump fluence above the P_{th} shows
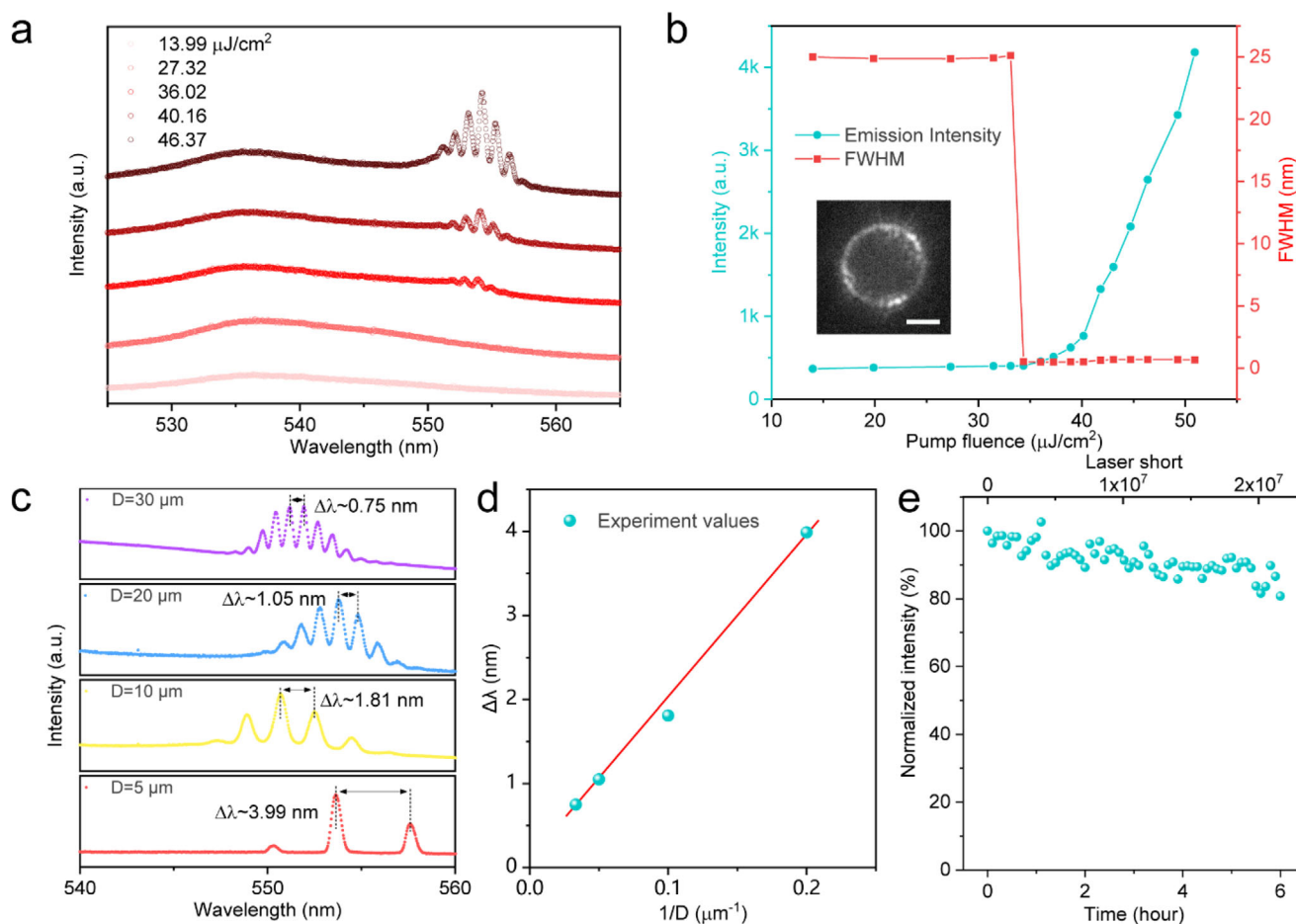
Figure 2. a) Emission spectra of individual MAPbBr$_3$ single-crystal microdisk with 20 μm diameter as a function of pump fluence. b) Pump fluence-dependent output emission intensity and FWHM of MAPbBr$_3$ single-crystal microdisk. Inset: Optical image of the microdisk emission with pump fluence above the lasing threshold. Scale bar, 5 μm. c) Emission spectra of single-crystal MAPbBr$_3$ microdisks with different diameters and the measuring mode spacing Δλ. d) The experimental Δλ as a function of $1/D$, where D is the diameter of microdisks. e) Time-dependent normalized lasing intensity under continuous excitation of $1.1P_{th}$ at ambient conditions.

interference patterns (the inset of Figure 2b), further confirming the lasing operation.

The lasing properties of MAPbBr$_3$ single-crystal microdisks with different diameters are further studied. The FSR, namely the axial mode spacing (Δλ), can be calculated as $\Delta\lambda = \lambda^2/\pi D n_{eff}$ for microdisk resonator theoretically, where n_{eff} is the effective refractive index of the microcavities, D is the diameter of microdisk, and λ is the resonant wavelength. From the emission spectra of microdisks with different diameters above the threshold in Figure 2c, it can be seen that as the diameter decreases from 30 to 5 μm, the mode spacing increases from 0.75 to 3.99 nm alone with less mode numbers. More deeply, the experimentally obtained Δλ is linearly proportional to the inverse of the diameter, as shown in Figure 2d, agreeing well with the FSR formula mentioned above. The effective refractive indices calculated from the experimental results are 4.89, 5.34, 4.65, and 4.3, respectively, which are consistent with the previously reported values.[33]

For inorganic/organic hybrid perovskite single-crystal microcavities, long-term operation stability is a prominent characteristic compared with polycrystalline films. Here, the normalized

lasing intensity under continuous excitation of $1.1P_{th}$ for up to 6 h at ambient condition is recorded in Figure 2e. It can be seen that the output intensity falls to 81% after 2.16×10^7 excitation cycles, which is comparable to the stability of all-inorganic perovskite quantum dots.[34] The outstanding stability originates from the single-crystal characterization against light, heat, and moisture.

In light-emitting devices, light-induced carrier dynamics, including hot carrier cooling, electron-hole recombination, and so on, play important roles in their optoelectronic performance. Here, we study the time-resolved emission dynamics in individual MAPbBr$_3$ microdisks including PL and lasing emission using the microscopic optical Kerr-gating technique (Figure S4, Supporting Information). The PL emission dynamics below the threshold is given in Figure S6 (Supporting Information). The emission intensity decay exponentially with two fast lifetimes of 1.61 and 86.97 ps, as well as a slow lifetime of 22.76 ns. This slow decay process could match the bulky recombination lifetime of 20.02 ns measured by TRPL in Figure 1f. In addition, the fast decay processes can be detected using the Kerr-gating technique, which provides a platform for the study of ultra-fast lasing dynamics.
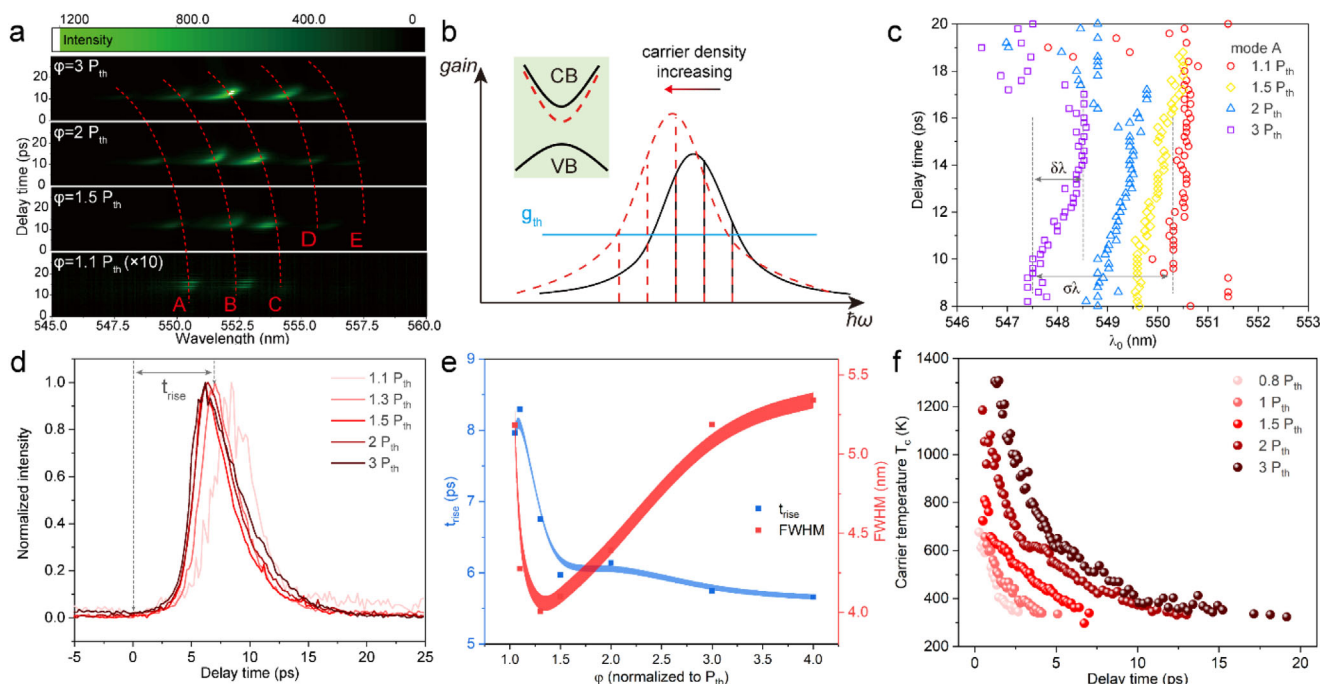
ADVANCED
SCIENCE NEWS

www.advancedsciencenews.com

LASER
& PHOTONICS
REVIEWS

www.lpr-journal.org

Figure 3. a) 2D pseudo-color plots of emission spectra under different pump fluences. The diameter of the studied microdisk is 5 μm and P_{th} is ≈63.48 μJ cm^{-2}. b) Gain spectra and energy diagram for lasing mechanism. Black solid lines: low pump fluence, red dashed lines: high pump fluence. c) The peak wavelength of mode A as a function of delay time under different pump fluences. d) Time-resolved emission dynamics of individual MAPbBr$_3$ single-crystal microdisk as a function of pump fluence. e) The error band of pulse t_{rise} and FWHM of emission versus pump fluence. The shaded areas depict the measurement uncertainties. f) Calculated time-dependent T_e with variable initial pump fluence.

Further insight into lasing properties of individual microcavity comes from time-resolved emission spectra. Since the optoelectronic behaviors are closely related to the light-induced carrier densities, the emission dynamics at different pump fluence above the threshold are investigated. As shown in the time-resolved emission spectra in **Figure 3a**, the observed lasing modes are labeled as modes A to E, corresponding to the emission wavelength increasing. It can be seen that several lasing modes (modes D and E) update on the long-wavelength side of the emission spectra with pump fluence increasing from $1.1P_{th}$ to $3P_{th}$, namely light-induced carrier density increasing. At the same time, the intensity proportions of the long-wavelength modes enhance as the pump fluence increases, as shown in Figure S7 (Supporting Information). More long-wavelength modes arise and dominate in the lasing emission with the pump fluence increasing, implying a red-shift of lasing gain profile.

To understand the evolution of gain profile as light-induced carrier density, a sketch of gain curves and energy diagram could be given in Figure 3b according to previous works.[35] The black solid lines and red dashed lines correspond to the low and high carrier density, respectively. It is well-known that bandgap renormalization, which decreases monotonically, occurs with increasing photoexcited carrier density.[21] This effect shifts the gain profile towards the low energy side, namely red-shift, as pump fluence increases. Another blue-shift of the gain profile is observed with time going on in Figure S8 (Supporting Information). It could be seen that for modes A and E, they share the approximative built-up time but different ending times. The phenomenon could be explained by the recombination of electron-

hole pairs over time, resulting in the decrease of light-induced carrier density.

Besides the gain profile variation with the carrier density, the wavelength of each resonant mode also changes with the pump fluence as indicated by the dashed line in Figure 3a. The peak wavelength of resonant modes (λ_0) as a function of delay time and pump fluence is given in detail in Figure 3c and Figure S9 (Supporting Information). There are ≈2–3 nm blue-shifts ($\sigma\lambda$, labeled in Figure 3c and Figure S10a, Supporting Information) of lasing resonant modes as pump fluence increases from $1.1P_{th}$ to $3P_{th}$, and 0.2-1.1 nm red-shifts ($\delta\lambda$) with time going on, which is associated with light-induced carrier dynamics. It is well known that the effective refractive index n_{eff} decrease with carrier density increases. Besides, the resonant wavelength depends on the effective refractive index, which could be expressed as $\lambda_0/n_{eff} = const$. Therefore, the lasing resonant modes shift to the higher energy side with pump fluence increasing and to the lower energy side with delay time elapsed. Moreover, the $\delta\lambda$ is proportional to the pump fluence as shown in Figure S10b (Supporting Information). It is expected that higher pump fluence results in a larger light-induced carrier density gradient.

The temporal behaviors of the emission pulses are also related to the pump fluence and light-induced carrier density, as shown by the integrated time-resolved emission in Figure 3d. The built-up time t_{rise} of emission, which is defined as the relative difference between the zero-delay time and delay time of emission maximum, decreases and eventually keeps constant with pump fluence increasing (Figure 3e). Meanwhile, the pump fluence-dependent FWHM, which depicts the pulse duration of
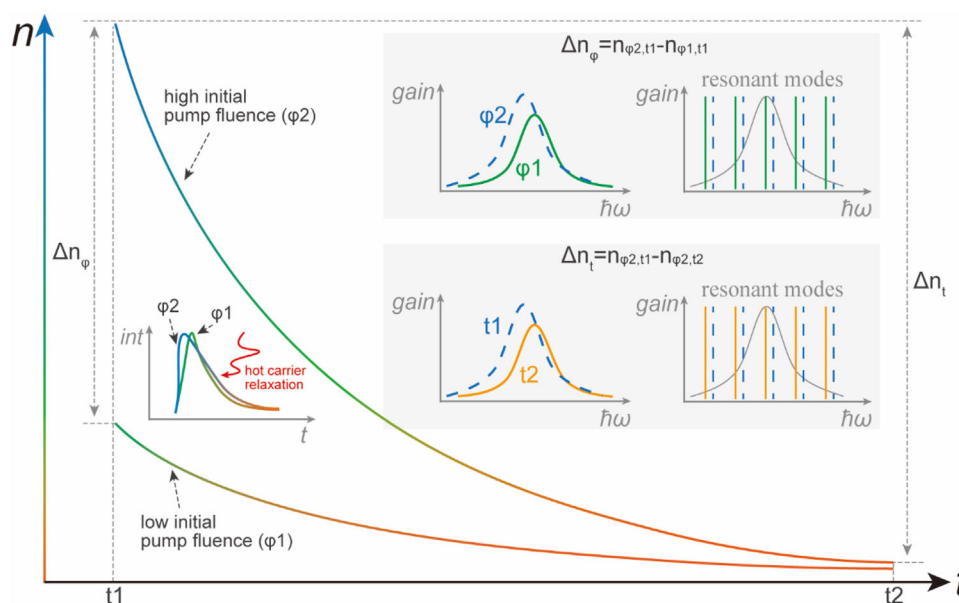
**ADVANCED
SCIENCE NEWS**

www.advancedsciencenews.com

LASER
& PHOTONICS
REVIEWS

www.lpr-journal.org

Figure 4. Schematic diagram of lasing spectral and temporal dynamics, which depend on the light-induced carrier density n.

microdisk lasing, reverses with the saturation of t_{rise}, as shown in Figure 3e. The decreasing of t_{rise} ($\varphi \leq 1.5P_{th}$) with pump fluence increasing originates from the accelerated relaxation of more collisional processes at higher carrier density, which shows that the excited carrier density is high enough to form population inversion, and the optical gain is independent of the relaxation/cooling behavior of high-energy electron-hole plasma. In the subsequent saturation stage of t_{rise}, the FWHM shows an abnormal tendency to extend. The widening of FWHM might originate from the long lifetime of hot carriers up to tens of picoseconds. Here, we evaluated the hot carrier lifetime based on femtosecond time-resolved transient absorption (fs-TA) measurement.

Figure S11 (Supporting Information) shows the TA spectra of MAPbBr$_3$ single-crystal as a function of pump fluence. The pump fluence-dependent hot carrier lifetimes are given in Figure 3f by fitting the high energy tail of TA photobleaching singles with Boltzmann distribution function $\Delta A(E) = -A_0(E)EXP(-E/k_BT_e)$, where k_B is the Boltzmann constant, T_e is the hot carrier temperature.[34] The lifetime of hot carriers ranges from several picoseconds to tens of picoseconds, depending on the pump fluence. As light-induced carrier density increases, phonon bottlenecks would lead to slow hot carrier cooling.[36,37] The evolution of hot carrier lifetime explains the widening of pulse duration FWHM with pump fluence exceeding $1.5P_{th}$. Based on the optical Kerr-gating technique and fs-TA measurement, the relationship between light-induced carrier density and lasing emission properties, including temporal behaviors, emission spectra shift, and mode evolution are clarified.

The discussions above give an understanding of the emission dynamics, including gain profile shift and lasing resonant modes evolution as a function of pump fluence and delay time. And the lasing temporal behavior, including build-up time and pulse duration, is also affected by the pump fluence. These behaviors are determined by the light-induced carrier density essentially. Thus, a schematic diagram is given in **Figure 4** to summarize the de-

pendence of emission dynamics on carrier density. Firstly, pump fluence decides the initial photoexcited carrier density, which would lead to the renormalization of the bandgap and the shift of the gain profile. Therefore, a red-shift of the lasing spectrum is observed with pump fluence increasing. Then, the evolution of photoexcited carrier density with time going on is given in a simple exponential decay. With time going on, the photoexcited carrier density decreases and results in the blue-shift of the gain profile. During this process, the lasing resonant modes shift to the long wavelength side due to the increment of effective refractive index. About the lasing temporal behavior, the pump fluence would act on the emission built-up time and pulse duration. Surprisingly, the broadening of pulse duration is observed since the built-up time reaches saturation, which is attributed to the long lifetime hot carriers in perovskite.

The transient spectral evolutions of perovskite lasing are revealed through photoexcited carrier density-dependent gain profiles and resonant modes. However, the insights into lasing dynamics in the space domain are lacking, while the local photoresponse and electroresponse are extensively reported in LEDs and photovoltaic devices.[38–40] Here, the spatial lasing dynamics in an individual microdisk are probed and mapped using the microscopic optical Kerr-gating image technique. As shown in **Figure 5a**, the emission intensity scattering from the sidewalls of a single microdisk is photoed as a function of delay time, from which the local lasing dynamics would be extracted. For example, three emission dynamics curves of different locations in the space domain are listed in Figure 5c. It is obvious that they present heterogeneous transient behaviors, mainly t_{rise}. By tracking the features of place I, II, and III labeled in Figure 5b, we find that the lasing t_{rise} is shortened as scattering light intensity increases. The scattering lights originate from the imperfect limitation of light due to the structural imperfections of cavity sidewalls, and brighter scattering light implies weaker light limitation and more optical loss. Since the optical gains only occur in the
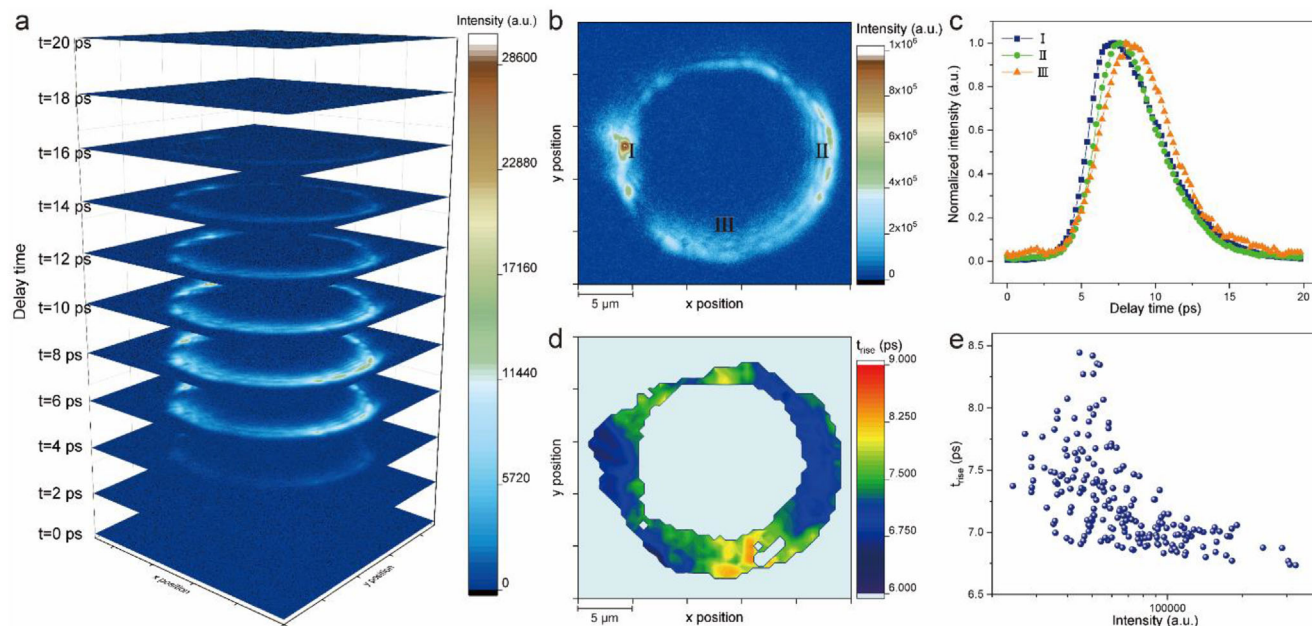
**ADVANCED
SCIENCE NEWS**

www.advancedsciencenews.com

LASER
& PHOTONICS
REVIEWS

www.lpr-journal.org

Figure 5. a) Temporal-spatial-resolved emission intensity map of MAPbBr$_3$ single-crystal microdisk with a diameter of 20 µm and pump fluence of ≈103.6 µJ cm^{-2}. b) Time-integral emission intensity map from Figure 5a. c) Normalized lasing dynamics extracted from the temporal-spatial-resolved emission images. The extractive positions are labeled in Figure 5b. d) Calculated lasing built-up time t_{rise} map fitted by Bigaussian function. The t_{rise} is adopted only when R^2 is greater than 0.99. e) The fitting t_{rise} as a function of emission intensity.

planes of circles for microdisks supported WGM modes, the microdisk could be divided into 2D planes with quantitative structural imperfections. For those planes with more imperfections and higher optical loss, more gains are required for population inversion, which means higher light-induced carrier density. As studied in Figures 3e and 4, the increasing of photoexcited carrier density would cause the shortening of lasing t_{rise}. Therefore, different gain thresholds and carrier densities due to the irregular structural imperfections vary the lasing dynamics for each two-dimensional plane. The global fitting t_{rise} map of individual MAPbBr$_3$ microdisk lasing and the t_{rise} scatter diagram as a function of emission intensity is shown in Figure 5d,e. It could be seen that lasing t_{rise} is inverse to the emission intensity on the whole. Consequently, the spatial heterogeneous lasing dynamics of individual microdisks are observed, which are attributed to the non-uniform optical losses and photoexcited carrier densities driven by the cavity structural imperfections.

3. Conclusion

In summary, we fabricate single-crystal MAPbBr$_3$ microcavities with customizable geometries and sizes using template-limited combined with anti-solvent diffusion growth method. These microcavities present a lasing threshold of ≈35 µJ cm^{-2}, and a quality factor of 1135, as well as excellent long-term operation stability. Microscopic optical Kerr-gating technique with sub-picosecond temporal resolution and sub-micron spatial resolution is used to explore the temporal-spatial evolution of the lasing process in individual microcavities. The band-gap renormalization, emission spectra shift, and other temporal behaviors as a function of injected light-induced carrier density are clarified. In addition, the spatial heterogeneous lasing dynamics in individual

microdisks are observed and attributed to the non-uniform structural imperfections on sidewalls. These results offer more references for the control of lasing behaviors in ultrafast time scale in perovskite microlasers.

4. Experimental Section

Synthesis of MAPbBr$_3$ Single-Crystal Microcavities: The MAPbBr$_3$ single-crystal microcavities were synthesized by a template-limited combination with anti-solvent diffusion growth method. The perovskite precursor solution (0.5 M) was configured by mixing methylammonium bromide (CH$_3$NH$_3$Br, 99.5%, Xi'an Baolaite) and Lead (II) bromide (PbBr$_2$, 99%, Meryer) with N,N-dimethylformamide (DMF, >99.9%, Aladdin). The stirred transparent solution was tightly confined between the silicon template and quartz substrate. The photolithographic silicon templates were treated by Trichloro-1H,1H,2H,2H-perfluorooctylsilan (>97.0%, Aladdin) for hydrophobic surfaces. The entirety was placed in a sealed container filled with 20 mL toluene (≥99.5%, Sinopharm) at room temperature for 12 h. When toluene vapor diffused into DMF, nucleation and growth of single-crystal perovskite at a slow rate happened since toluene is a poor solvent for MAPbBr$_3$.

Temporal-Spatial-Resolved PL and Lasing Measurements: The temporal-spatial-resolved emission measurements were performed on a home-built micro-PL set-up as shown in Figure S4 (Supporting Information). The fundamental laser pulses (central wavelength: 800 nm, pulse width: 50 fs, and repetition rates: 1 kHz) were derived from a Ti: sapphire laser system, which were then divided into two beams. The stronger part was used as the gating beam to trigger birefringence in the nonlinear Kerr medium, and the other part's frequency was doubled generating a 400 nm excitation beam for lasing emission. The 400 nm excitation pulses were focused onto the sample with a microscope objective (40×, NA = 0.75). To ensure uniform excitation across the entire single-crystal MAPbBr$_3$ microcavity, the laser beam size was optimized by adjusting the distance between the sample and the microscope objective. Then the emission from microcavity after passing through the linear polarizer was focused into an optical Kerr

medium, CS_2, together with the gating pulse that was variably delayed by an optical delay line. The gating pulses induced a transient birefringence in the optical Kerr medium, and the polarization of the emission signal was rotated and parts of the light passed through the analyzer. By adjusting the delay time between the pump and probe pulses, the temporal and spatial evolution of the emission from individual microcavity could be recorded by the spectrometer and CCD, respectively. The spatial and temporal resolutions of the microscopic optical Kerr gating measurements were estimated to be better than 0.8 μm and 300 fs, respectively.

Femtosecond Time-Resolved Transient Absorption Measurements: The transient absorption spectra were achieved by a home-built TA set-up with about 100 fs time resolution. The fundamental laser pulses (central wavelength: 800 nm, pulse width: 50 fs, and repetition rates: 1 kHz) were split into two beams; the stronger one was frequency doubled generating a 400 nm pump light, and the other one was focused into a sapphire plate producing the broadband supercontinuum probe light. The pump and probe pulses were focused into the sample simultaneously, and the transmitted probe light was recorded by a spectrometer. By changing the delay time between the pump and probe pulses through a translation stage, time-resolved transient absorption spectra were obtained.

Characterizations: The morphological characterizations and crystal structure of single-crystal $MAPbBr_3$ microcavities were measured by an optical microscope (DS-Fi3, Nikon, Japan), scanning electron microscope (Quanta 250FEG, FEI, USA), atomic force microscope (INNOVA, Bruker, Germany), and X-ray diffraction spectrometer (Cu Kα radiation, D8 Advance, Bruker, Germany). The absorption spectrum was measured by an UV-1800 spectrophotometer (Shimadzu, Japan). TRPL data were recorded by a fluorescence spectrometer (FLS980, Edinburgh Instrument, UK) equipped with a 375 nm laser.

Supporting Information

Supporting Information is available from the Wiley Online Library or from the author.

Conflict of Interest

The authors declare no conflict of interest.

Data Availability Statement

The data that support the findings of this study are available from the corresponding author upon reasonable request.

[1] C. Huang, C. Zhang, S. Xiao, Y. Wang, Y. Fan, Y. Liu, N. Zhang, G. Qu, H. Ji, J. Han, L. Ge, Y. Kivshar, Q. Song, *Science* **2020**, *367*, 1018.

[2] J. Wang, S. Paesani, Y. Ding, R. Santagati, P. Skrzypczyk, A. Salavrakos, J. Tura, R. Augusiak, L. Mančinska, D. Bacco, D. Bonneau, J. W. Silverstone, Q. Gong, A. Acín, K. Rottwitt, L. K. Oxenløwe, J. L. O'Brien, A. Laing, M. G. Thompson, *Science* **2018**, *360*, 285.

[3] X. Cai, J. Wang, M. J. Strain, B. Johnson-Morris, J. Zhu, M. Sorel, J. L. O'Brien, M. G. Thompson, S. Yu, *Science* **2012**, *338*, 363.

[4] J. P. Epping, T. Hellwig, M. Hoekman, R. Mateman, A. Leinse, R. G. Heideman, A. van Rees, P. J. van der Slot, C. J. Lee, C. Fallnich, K. J. Boller, *Opt. Express* **2015**, *23*, 19596.

[5] C. Zhang, C.-L. Zou, H. Dong, Y. Yan, J. Yao, Y. S. Zhao, *Sci. Adv.* **2017**, *3*, e1700225.

[6] J. Zhao, Y. Yan, Z. Gao, Y. Du, H. Dong, J. Yao, Y. S. Zhao, *Nat. Commun.* **2019**, *10*, 870.

[7] H. Zhao, P. Miao, M. H. Teimourpour, S. Malzard, R. El-Ganainy, H. Schomerus, L. Feng, *Nat. Commun.* **2018**, *9*, 981.

[8] Q. Bao, W. Li, P. Xu, M. Zhang, D. Dai, P. Wang, X. Guo, L. Tong, *Light: Sci. Appl.* **2020**, *9*, 42.

[9] Y. Jiang, Y. Y. Liu, X. Liu, H. Lin, K. Gao, W. Y. Lai, W. Huang, *Chem. Soc. Rev.* **2020**, *49*, 5885.

[10] M. Tuo, C. Xu, H. Mu, X. Bao, Y. Wang, S. Xiao, W. Ma, L. Li, D. Tang, H. Zhang, M. Premaratne, B. Sun, H.-M. Cheng, S. Li, W. Ren, Q. Bao, *ACS Photonics* **2018**, *5*, 1808.

[11] Y. Fu, J. Cao, K. Yamanouchi, H. Xu, *Ultrafast Sci.* **2022**, *2022*, 9867028.

[12] Y. Fu, H. Zhu, J. Chen, M. P. Hautzinger, X.-Y. Zhu, S. Jin, *Nat. Rev. Mater.* **2019**, *4*, 169.

[13] Q. Zhang, Q. Shang, R. Su, T. T. H. Do, Q. Xiong, *Nano Lett.* **2021**, *21*, 1903.

[14] H. Zhu, Y. Fu, F. Meng, X. Wu, Z. Gong, Q. Ding, M. V. Gustafsson, M. T. Trinh, S. Jin, X. Y. Zhu, *Nat. Mater.* **2015**, *14*, 636.

[15] B. Tang, H. Dong, L. Sun, W. Zheng, Q. Wang, F. Sun, X. Jiang, A. Pan, L. Zhang, *ACS Nano* **2017**, *11*, 10681.

[16] Z. Liu, J. Yang, J. Du, Z. Hu, T. Shi, Z. Zhang, Y. Liu, X. Tang, Y. Leng, R. Li, *ACS Nano* **2018**, *12*, 5923.

[17] N. Zhang, W. Sun, S. P. Rodrigues, K. Wang, Z. Gu, S. Wang, W. Cai, S. Xiao, Q. Song, *Adv. Mater.* **2017**, *29*, 1606205.

[18] Y. Zhong, K. Liao, W. Du, J. Zhu, Q. Shang, F. Zhou, X. Wu, X. Sui, J. Shi, S. Yue, Q. Wang, Y. Zhang, Q. Zhang, X. Hu, X. Liu, *ACS Nano* **2020**, *14*, 15605.

[19] C. Xiao, Z. Li, H. Guthrey, J. Moseley, Y. Yang, S. Wozny, H. Moutinho, B. To, J. J. Berry, B. Gorman, Y. Yan, K. Zhu, M. Al-Jassim, *J. Phys. Chem. C* **2015**, *119*, 26904.

[20] J. Zhang, Q. Guo, X. Li, C. Li, K. Wu, I. Abrahams, H. Yan, M. M. Knight, C. J. Humphreys, L. Su, *ACS Nano* **2020**, *14*, 11029.

[21] A. P. Schlaus, M. S. Spencer, K. Miyata, F. Liu, X. Wang, I. Datta, M. Lipson, A. Pan, X. Y. Zhu, *Nat. Commun.* **2019**, *10*, 265.

[22] J. Wang, H. Yu, G. Liu, W. Liu, Y. Duan, X. Cheng, L. Dai, S. Wang, Q. Gong, *Adv Photonics Res* **2022**, *3*, 2100182.

[23] J. Wang, G. Liu, W. Liu, Y. Chen, X. Cheng, H. Yang, Y. Gao, L. Xiao, S. Wang, Q. Gong, *J. Phys. Chem. C* **2022**, *126*, 14922.

[24] H. Zhang, Q. Liao, Y. Wu, Z. Zhang, Q. Gao, P. Liu, M. Li, J. Yao, H. Fu, *Adv. Mater.* **2018**, *30*, 1706186.

[25] H. Zhang, Y. Wu, Q. Liao, Z. Zhang, Y. Liu, Q. Gao, P. Liu, M. Li, J. Yao, H. Fu, *Angew. Chem., Int. Ed. Engl.* **2018**, *130*, 7874.

[26] Y. Chen, H. Zeng, P. Ma, G. Chen, J. Jian, X. Sun, X. Li, H. Wang, W. Yin, Q. Jia, G. Zou, *Angew. Chem., Int. Ed. Engl.* **2021**, *133*, 2661.

[27] W. Peng, L. Wang, B. Murali, K. T. Ho, A. Bera, N. Cho, C. F. Kang, V. M. Burlakov, J. Pan, L. Sinatra, C. Ma, W. Xu, D. Shi, E. Alarousu, A. Goriely, J. H. He, O. F. Mohammed, T. Wu, O. M. Bakr, *Adv. Mater.* **2016**, *28*, 3383.

[28] H. Di, W. Jiang, H. Sun, C. Zhao, F. Liao, Y. Zhao, *ACS Omega* **2020**, *5*, 23111.

[29] D. Shi, V. Adinolfi, R. Comin, M. Yuan, E. Alarousu, A. Buin, Y. Chen, S. Hoogland, A. Rothenberger, K. Katsiev, Y. Losovyj, X. Zhang, P. A. Dowben, O. F. Mohammed, E. H. Sargent, O. M. Bakr, *Science* **2015**, *347*, 519.

[30] Z. Chen, Q. Dong, Y. Liu, C. Bao, Y. Fang, Y. Lin, S. Tang, Q. Wang, X. Xiao, Y. Bai, Y. Deng, J. Huang, *Nat. Commun.* **2017**, *8*, 1890.

[31] Y. Chen, G. Chen, Z. Zhou, X. Li, P. Ma, L. Li, W. Yin, H. Zeng, G. Zou, *Adv. Funct. Mater.* **2021**, *31*, 2101966.

[32] K. H. Wang, L. C. Li, M. Shellaiah, K. W. Sun, *Sci. Rep.* **2017**, *7*, 13643.

[33] S. Zhang, Q. Shang, W. Du, J. Shi, Z. Wu, Y. Mi, J. Chen, F. Liu, Y. Li, M. Liu, Q. Zhang, X. Liu, *Adv. Optical Mater.* **2018**, *6*, 1701032.

[34] C.-Y. Huang, C. Zou, C. Mao, K. L. Corp, Y.-C. Yao, Y.-J. Lee, C. W. Schlenker, A. K. Y. Jen, L. Y. Lin, *ACS Photonics* **2017**, *4*, 2281.

[35] C. Klingshirn, J. Fallert, H. Zhou, J. Sartor, C. Thiele, F. Maier-Flaig, D. Schneider, H. Kalt, *Phys. Status Solidi* **2010**, *247*, 1424.

[36] M. Li, J. Fu, Q. Xu, T. C. Sum, *Adv. Mater.* **2019**, *31*, 1802486.

[37] Y. Yang, D. P. Ostrowski, R. M. France, K. Zhu, J. van de Lagemaat, J. M. Luther, M. C. Beard, *Nat. Photonics* **2015**, *10*, 53.

[38] W. Li, S. K. Yadavalli, D. Lizarazo-Ferro, M. Chen, Y. Zhou, N. P. Padture, R. Zia, *ACS Energy Lett.* **2018**, *3*, 2669.

[39] Y. Kutes, Y. Zhou, J. L. Bosse, J. Steffes, N. P. Padture, B. D. Huey, *Nano Lett.* **2016**, *16*, 3434.

[40] Y. Wang, Z. Hu, W. Yao, C. Yang, H. Zhang, J. Zhang, Y. Zhu, *Appl. Phys. Lett.* **2020**, *117*, 083902.